

## The formation of asteroid satellites in large impacts: results from numerical simulations

Daniel D. Durda,<sup>a,\*</sup> William F. Bottke Jr.,<sup>a</sup> Brian L. Enke,<sup>a</sup> William J. Merline,<sup>a</sup> Erik Asphaug,<sup>b</sup>  
Derek C. Richardson,<sup>c</sup> and Zoë M. Leinhardt<sup>c</sup>

<sup>a</sup> Southwest Research Institute, 1050 Walnut Street Suite 400, Boulder, CO 80302, USA

<sup>b</sup> Earth Sciences Department, University of California Santa Cruz, Santa Cruz, CA 95064, USA

<sup>c</sup> Department of Astronomy, University of Maryland, College Park, MD 20742, USA

Received 27 June 2003; revised 15 September 2003

### Abstract

We present results of 161 numerical simulations of impacts into 100-km diameter asteroids, examining debris trajectories to search for the formation of bound satellite systems. Our simulations utilize a 3-dimensional smooth-particle hydrodynamics (SPH) code to model the impact between the colliding asteroids. The outcomes of the SPH models are handed off as the initial conditions for  $N$ -body simulations, which follow the trajectories of the ejecta fragments to search for the formation of satellite systems. Our results show that catastrophic and large-scale cratering collisions create numerous fragments whose trajectories can be changed by particle–particle interactions and by the reaccretion of material onto the remaining target body. Some impact debris can enter into orbit around the remaining target body, which is a gravitationally reaccreted rubble pile, to form a SMASHed Target Satellite (SMATS). Numerous smaller fragments escaping the largest remnant may have similar trajectories such that many become bound to one another, forming Escaping Ejecta Binaries (EEBs). Our simulations so far seem to be able to produce satellite systems qualitatively similar to observed systems in the main asteroid belt. We find that impacts of 34-km diameter projectiles striking at  $3 \text{ km s}^{-1}$  at impact angles of  $\sim 30^\circ$  appear to be particularly efficient at producing relatively large satellites around the largest remnant as well as large numbers of modest-size binaries among their escaping ejecta.

© 2003 Elsevier Inc. All rights reserved.

*Keywords:* Asteroids; Collisional physics; Impact processes; Satellites, general

### 1. Introduction

The main asteroid belt has long been recognized as a “natural laboratory” for understanding diverse impact outcomes and on-going collisional evolution (e.g., Davis et al., 1979, 1985, 1989). The exciting discoveries of what is now a growing suite of main-belt asteroid satellites<sup>1</sup> (Merline et al.,

2002a) have renewed interest in the diversity of collisional mechanisms that may lead to the formation of small-body satellites and binary pairs. Since collisions are the dominant evolutionary process affecting asteroids, it is plausible that these satellites are by-products of cratering and/or catastrophic disruption events.

Understanding how asteroid satellites form is important because:

- (1) they hold important clues to both the past and present collisional environment of the main asteroid belt;
- (2) models of their formation may provide constraints on internal structures of asteroids beyond those possible from observations of satellite orbital properties alone;

3-body exchange reactions to form KBO binaries in the primordial Kuiper belt, their mechanism invokes collisionally-formed binaries like those studied here as a starting condition.

\* Corresponding author.

*E-mail address:* [durda@boulder.swri.edu](mailto:durda@boulder.swri.edu) (D.D. Durda).

<sup>1</sup> A number of satellites have been discovered in the near-Earth asteroid (NEA) and Kuiper belt object (KBO) populations as well. However, several mechanisms other than direct, physical, 2-body collisions have been invoked to explain their origin. NEA satellites are likely produced by tidal disruption after close approaches to the terrestrial planets (Bottke and Melosh, 1996a, 1996b; Richardson et al., 1998) and the large KBO satellites observed to date appear to have formed in primordial times through various dynamical mechanisms (Weidenschilling, 2002; Goldreich et al., 2002; Funato et al., 2003). Note, however, that although Funato et al. (2003) invoke

- (3) they represent numerous small-scale potential analogs for the early, large impacts believed responsible for the formation of the Earth–Moon and Pluto–Charon systems.

Initial models for asteroid satellite formation have utilized basic analytic arguments and simple numerical investigations (see Weidenschilling et al., 1989; Merline et al., 2002a, for reviews). These studies have identified several collisional processes as plausible formation mechanisms; these include:

- (1) mutual capture following catastrophic disruption;
- (2) rotational fission due to glancing impact and spin-up;
- (3) reaccretion in orbit of ejecta from large, non-catastrophic impacts.

Here we present results from a systematic numerical investigation directed toward mapping out the parameter space of the three collisional mechanisms described above. To date we have focused on mechanisms 1 and 3, and in this paper we present results on the ‘global’ statistical properties of the satellite systems formed in our numerical simulations (number of satellites per event, size of the largest satellite, etc.). In a subsequent paper we will discuss the statistical properties of satellites formed in the individual simulations (distribution of semimajor axes, eccentricities, etc.).

## 2. Numerical technique

Hartmann (1979) was probably the first to suggest that the complete fragmentation of a parent asteroid might result in the ejection of some fragments with very similar velocities, resulting in mutual capture between ejected fragments into gravitationally bound pairs. Durda (1996) conducted a first-look numerical study of this mechanism by performing three-dimensional  $N$ -body integrations of fragments in the initial stages of the expanding debris field resulting from the disruption of a parent asteroid. In that early model, no physics accounting for the impact event or fracturing was included; the parent “asteroid” was instead empirically treated as a strengthless rubble pile made up of spherical components that were each assumed to be of infinite strength. The simulation began with a target body composed of a fragmentation power-law size distribution of up to  $\sim 6000$  spherical fragments (the largest with  $D \approx 63$  km), all initially contained within the volume of a 110-km diameter parent asteroid (the size of the parent object of the Koronis asteroid family (Zappalà et al., 1984)). All fragments were launched away from the target’s center according to mass-speed distributions matching that observed for members of the Koronis family. Low-speed collisions between particles were treated as partially elastic collisions, so that particles simply “bounced” off each other with reduced speeds. Fragment trajectories were integrated for up to 72 h after the assumed

disruption event and continuously monitored to search for the formation and dissolution of bound pairs.

The major findings of the Durda (1996) study were:

- (1) bound asteroid pairs were produced in each of the dozens of simulations;
- (2)  $< 10\%$  of the original parent asteroid’s mass ended up in gravitationally bound pairs, either involving orbiting or contact configurations;
- (3) a variety of morphological types of bound pairs resulted, ranging from very large primaries with tiny satellites (like Ida/Dactyl) to small binary pairs with equal-size components.

Dorissoundiram et al. (1997) reached very similar conclusions in an independent study using a similar  $N$ -body model with semiempirically derived initial conditions.

Here, we substantially improve upon these earlier models by taking advantage of state-of-the-art numerical tools that have not been applied in previous asteroid satellite formation studies. These include:

- (1) smooth-particle hydrodynamics (SPH) codes, which model the pressures, temperatures, and energies of asteroid–asteroid impacts;
- (2) efficient  $N$ -body codes, which can track the trajectories of hundreds-of-thousands of individual collision fragments in an expedient manner.

Simulations using SPH codes are used to model impacts between colliding asteroids. When the impact simulations are complete (crater formation/ejecta flow fields established with no further fragmentation/damage), the outcomes of the SPH models are handed off as the initial conditions for  $N$ -body simulations, which follow the trajectories of the ejecta fragments for an extended time to search for the formation of bound satellite systems. This is essentially the same numerical scheme utilized by Michel et al. (2001, 2002) to study the formation of asteroid families. Note that these authors also found that satellites seem to form naturally as a result of collisions and have also presented results on the number of satellites formed as a function of different impact regimes.

Below, we briefly summarize the SPH and  $N$ -body simulation techniques.

### 2.1. Smooth-particle hydrodynamic simulations

We modeled the initial stages of large impacts between two asteroids with the 3D SPH code SPH3D (Benz and Asphaug, 1995). SPH3D models shock propagation in elastic solids, utilizing a plastic yield criterion for intense deformation together with an explicit fracture and dynamic fragmentation model acting on the principal tensile component of the stress tensor during brittle deformation. The results presented here are not sensitive to the parameters utilized in our

fragmentation model, as damage—the measure of the elastic strength—is total, throughout both impacting bodies, by the end of these calculations. The fracture model does, however, affect the coupling of impact energy into the target, including the behavior of the back spall zone. We adopt fracture parameters appropriate for terrestrial basalt (see Asphaug et al., 2003, for a table of these parameters). In future work we intend to utilize fracture parameters derived from ongoing experiments into chondritic meteorites (e.g., Flynn and Durda, 2002; Durda et al., 2002), although we do not expect the outcome to change significantly on that basis.

The equation of state model used is that of Tillotson (1962), which is based upon the linear relationship between shock speed and particle velocity (see Appendix II of Melosh, 1989, for a detailed description). While more sophisticated equations of state can be utilized, the Tillotson equation of state is well understood and gives excellent results in comparison to ejecta velocities derived from laboratory impact experiments (Benz and Asphaug, 1994, 1995).

For objects of the size considered in this study (i.e., the disruption of 100 km-scale objects), explicit treatment of gravity within the SPH code is not necessary since the time scale for shock propagation through the body and fragmentation is much shorter than the gravitational time scale (Asphaug, 1997). We do, however, incorporate gravitational self-compression of the target during the impact phase as an overburden stress that must be exceeded before fracture can initiate (Asphaug and Melosh, 1993). Generally speaking, the use of a Courant-limited compressible hydrocode, where the time step is governed by the inverse sound speed, is prohibitive for calculations of gravitational evolution of small bodies, whose escape speeds are a thousand times lower than the sound speed.<sup>2</sup> Thus, we use SPH only for the collision itself, and the evolution to a state where hydrodynamic flow attains equilibrium and is only further modified by self gravity.

For modeling the largest remnant of a collision with SPH, Benz and Asphaug (1995, 1999) found that  $\sim 40,000$  particles was adequate. Canup and Asphaug (2001) attained resolution convergence for the origin of Earth's Moon, in SPH calculations, with a similar number of particles. Our requirements here are stricter, because we are also interested not only in mass ejected but in pairing of ejecta to form satellite systems.

We ran a number of SPH simulations to determine the number of SPH particles that are needed to reach resolution convergence, that is, so that modeled collision outcomes (mass of largest fragment remnant, size distribution of the larger fragments, etc.) are not dependent on the number of SPH particles used to describe the target and projectile as-

teroids. We ran four simulations of the impact of a 20 km diameter projectile into a 100 km diameter target asteroid at  $5 \text{ km s}^{-1}$ , setting the physical parameters of each collision to be identical in each run, but with 50,000, 100,000, 200,000, and 528,000 SPH particles comprising the targets in each case. The number of particles in the impactor in each case was chosen such that the particle number density in the impactor was the same as in the target. We found that for targets with 100,000 or more particles the modeled collision outcomes matched each other sufficiently well that we concluded that we achieved resolution convergence for fragments a few to several kilometers in diameter. Note that the very smallest satellites generated in our models (particularly those consisting of only single SPH/ $N$ -body particles) are at or near the resolution limit of our simulations; their properties should not be considered particularly meaningful.

## 2.2. $N$ -body simulations

Once the impact simulations are complete (crater formation/ejecta flow fields established with no further fragmentation/damage), the outcomes of the SPH models are handed off as the initial conditions for  $N$ -body simulations, which follow the trajectories of the ejecta fragments for sufficient time to search for the formation of bound satellite systems. To track the trajectories of collision fragments we use a modified version of the cosmological  $N$ -body code `pkdgrav`, featured in Richardson et al., 2000, (also see Leinhardt et al., 2000; Leinhardt and Richardson, 2002). `pkdgrav` is a scalable, parallel tree code designed for ease of portability and extensibility, and is arguably the fastest code available for this type of simulation. A unique feature of this code is the ability to rapidly detect and accurately treat low-speed collisions between particles (with or without self-gravity), even at the extreme limits seen in dense granular media such as sandpiles. This allows for realistic modeling of the formation of rubble pile accumulations among ejected fragments.

The tree component of the code provides a convenient means of consolidating forces exerted by distant particles, reducing the computational cost. The parallel component divides the work evenly among available processors, adjusting the load each time step according to the amount of work done in the previous force calculation. The code uses a straight-forward second-order leapfrog scheme for the integration and computes gravity moments from tree cells to hexadecapole order. Particles are considered to be finite-sized hard spheres and collisions are identified during each time step using a fast neighbor-search algorithm. Low-speed collisions between debris fragments are treated as mergers resulting in a new spherical particle of appropriate combined mass and equivalent diameter.

The  $N$ -body simulations are run, with time steps equal to  $10^{-5}$  in units of  $\text{year}/2\pi$  (i.e.,  $\sim 50$  sec), to a time about 4 days (i.e., 7000 time steps) after the impact, thus simulating only the initial formation of bound satellites. Our choice of 4 days of  $N$ -body simulation time after impact

<sup>2</sup> In large-scale collisions, (e.g., Canup and Asphaug, 2001), escape speed and sound speed are comparable so the Courant condition is not restrictive to modeling dynamical evolution. Modeling the formation of asteroid satellites is in this sense more complex than modeling the formation of Earth's Moon.

was set by available CPU resources and limitations inherent in the simulations due to the fact that irregular primary asteroid shapes are not preserved and mutual tidal interactions are not included. Longer-term dynamical evolution of individual satellite systems may be examined in future studies with a version of `pkdgrav` that includes both these effects. Plots of the total number of satellites and the total number of bound satellite systems as a function of time after impact both show features that one would expect to see after a “sufficient” amount of simulation run time (i.e., by 4 days after impact):

- (1) both are well-behaved, decreasing functions of time;
- (2) there are only relatively small fluctuations in the number of satellites and satellite systems that one would expect to see due to formation and dissolution of transient binaries.

We use a hierarchical 3D spatial tree code (`companion`; Leinhardt and Richardson, in preparation) to search for bound pairs in the output. As with gravity tree codes, this method reduces the search cost to order  $N \log N$  by considering only nearby particles, or members of more distant particle groups with low relative bulk motion, as potential companions. The search is parameterized by a standard tree cell opening-angle criterion (e.g., Barnes and Hut, 1986); the default of 0.25 radian used in `companion` is quite conservative and is based on the assumption that searches will be conducted infrequently on a given data set. In principle very distant companions could be missed, but thorough testing shows that over 98% of binaries are found in most cases. Note that the current version of `companion` only searches for systems where the satellite is bound to one primary. It is possible that catastrophic collisions could produce more complex multiple systems where the satellite is bound to more than one primary—such systems would not be detected by the current analysis.

### 2.3. ‘Handoff’ between SPH and $N$ -body simulations

Converting the SPH3D output into input parameters for `pkdgrav` is a multi-step process. To make our simulations numerically feasible, some simplifications were made.

First, we had to account for the fact that the SPH ‘particles’ are not really particles, but instead represent overlapping Gaussian distributions with fixed densities. When these particles are converted into the hard-sphere particles utilized in `pkdgrav`, they cannot maintain the same density or size because `pkdgrav` cannot account for mutual overlapping particles. To overcome this problem, we modified the size and volume of each `pkdgrav` particle, ensuring that mass is conserved. Thus, the initial size of each `pkdgrav` particle is smaller than that in the SPH code, while their densities are slightly higher.

Second, we assume that all collisions result in accretion, reasonable for most of the particle relative speeds of interest

(less than tens of  $\text{m s}^{-1}$ ). When particles collide, we force them to merge into a single body. This approximation frequently compels most of the particles in the target body to merge into a single particle before the end of the simulation. We do this to avoid having to compute numerous collisions between adjacent bodies that have essentially zero speeds. When the merger events take place, we use conservation of mass and volume to reset the particles back to the sizes and densities they had back in the SPH code. Thus, an unperturbed target body started in `pkdgrav` will collapse slightly onto itself (a by-product of using smaller particle sizes) before merging into a single particle and swelling back up to the diameter it had in the SPH code.

## 3. Results and discussion

To date we have run 161 SPH/ $N$ -body simulations of impacts onto 100-km diameter target asteroids (Durda et al., 2003). The non-rotating targets are assumed to be spherical and are composed of solid basalt with a density of  $2.7 \text{ g cm}^{-3}$  (yielding a target mass of  $1.414 \times 10^{18} \text{ kg}$ ). The spherical basalt impactors range in diameter from 10 to 46 km, impact speeds range from 2.5 to  $7 \text{ km s}^{-1}$ , and impact angles range from  $15^\circ$  to  $75^\circ$  (nearly head-on to very oblique) in  $15^\circ$  increments. We conducted some additional simulations with larger impactors and intermediate impact speeds and impact angles (e.g., 63-km diameter impactors, impacts at speeds of 2.5 and  $3.5 \text{ km s}^{-1}$ , and impact angles of  $25^\circ$ ,  $35^\circ$ , and  $40^\circ$ ). Initial conditions and results for all 161 simulations are summarized in Table 1.

Our scheme for setting up the SPH simulations with various impact angles was to (1) pick an impact angle,  $\theta$ , and then (2) position the center of the impactor a distance  $R = R_{\text{targ}} + R_{\text{imp}}$  away from the center of the target, where  $R_x = R \cos(\theta)$ ,  $R_y = R \sin(\theta)$ , and  $R_z = 0$ . In practice, we also added to  $R$  a small additional separation of 2 km so that the SPH particles in the target and impactor were not overlapping at the very first time step. The impact angle  $\theta$  is measured, at the target sphere’s surface, between the impactor velocity vector (which is in the negative  $x$  direction in all the simulations) and the line connecting the centers of the target and impactor, so that  $\theta = 0^\circ$  corresponds to a head-on impact and  $\theta = 90^\circ$  is the end-member oblique impact. In the extreme case of a very large target and a very small projectile, this definition becomes the same as is usually assumed for half-plane impacts. Results from impact cratering experiments (Anderson et al., 2002) show that craters are symmetrical for oblique impacts, but not about the impact point: the center of deposition of energy is shifted down-range from the contact point. For oblique impacts between spheres, as in our simulations here, one might expect the characteristic of the impact to be shifted to a higher effective impact angle than the angle  $\theta$  that we have defined here.

Our results show that energetic (i.e., catastrophic) collisions create numerous fragments whose orbits can be

Table 1  
Results of 161 SPH/*N*-body simulations

Impact speed (km s <sup>-1</sup> )	Impact angle (deg)	log( $M_{\text{targ}}/M_{\text{imp}}$ )	Largest remnant diameter (km)	$M_{\text{Ir}}/M_{\text{targ}}$	Number of SMATS <sup>a</sup>	SMATS equivalent diameter (km)	Number of EEB primaries	Number of EEB secondaries	Largest EEB primary (km)	Largest EEB secondary (km)
2.5	30	1.4	72.37	0.3791	13(2)	5.54	693	946	22.33	12.14
3	15	1.0	14.89	0.0033	0	–	533	550	9.72	4.48
3	15	1.4	22.82	0.0119	18(2)	5.85	890	1148	22.31	7.49
3	15	1.8	71.67	0.3681	2(0)	2.71	823	931	16.62	9.21
3	15	2.2	90.80	0.7485	2(0)	2.71	362	388	11.32	4.12
3	15	2.6	97.41	0.9241	0	–	38	43	6.38	3.11
3	15	3.0	99.14	0.9742	0	–	13	13	6.77	2.71
3	25	1.4	49.43	0.1208	82(19)	11.77	1037	1297	19.84	13.04
3	30	1.0	12.49	0.0019	0	–	1156	1283	10.91	5.07
3	30	1.2	18.95	0.0068	22(7)	8.79	1455	1966	16.81	6.98
3	30	1.4	55.70	0.1728	92(17)	13.46	1070	1406	29.20	9.04
3	30	1.6	70.92	0.3568	6(3)	5.65	973	1215	16.20	7.66
3	30	1.8	82.31	0.5576	7(0)	4.12	666	834	14.49	7.61
3	30	2.2	94.08	0.8327	1(1)	3.11	193	211	9.62	3.11
3	30	2.6	97.76	0.9341	0	–	42	48	10.74	3.91
3	30	3.0	99.21	0.9765	0	–	8	8	2.71	2.15
3	35	1.4	63.96	0.2616	111(27)	17.13	1050	1346	21.57	6.91
3	45	1.0	66.09	0.2886	22(3)	6.30	608	817	21.98	8.29
3	45	1.4	81.82	0.5477	8(0)	4.31	393	531	19.11	12.74
3	45	1.8	91.50	0.7659	3(1)	4.48	236	256	11.89	5.19
3	45	2.2	95.88	0.8814	0	–	127	141	9.13	5.1
3	45	2.6	98.62	0.9591	0	–	20	22	6.98	6.38
3	45	3.0	99.48	0.9845	0	–	2	2	2.15	2.15
3.5	30	1.4	27.16	0.0200	47(9)	8.57	1252	1780	19.95	7.18
3	60	1.0	89.94	0.7274	0	–	228	265	14.03	6.84
3	60	1.4	94.20	0.8359	0	–	160	186	26.91	4.12
3	60	1.8	96.56	0.9003	0	–	73	84	12.12	4.64
3	60	2.2	98.44	0.9538	0	–	20	20	3.42	2.71
3	60	2.6	99.31	0.9793	0	–	2	2	2.15	2.15
3	60	3.0	99.71	0.9912	0	–	1	1	2.15	2.15
3	75	0.6	98.82	0.9650	0	–	23	25	6.21	2.71
3	75	1.0	99.39	0.9818	0	–	7	7	3.91	2.71
3	75	1.4	99.70	0.9910	0	–	8	26	26.76	5.07
3	75	1.8	99.76	0.9927	0	–	4	5	23.01	6.62
3	75	2.2	99.85	0.9955	0	–	4	4	4.48	2.15
3	75	2.6	99.92	0.9976	0	–	0	0	–	–
3	75	3.0	99.95	0.9983	0	–	0	0	–	–
4	15	1.0	8.62	0.0006	0	–	175	176	5.85	3.68
4	15	1.4	15.77	0.0039	1(0)	2.15	432	443	14.60	4.31
4	15	1.8	38.44	0.0568	42(9)	8.75	678	956	31.54	7.31
4	15	2.2	79.04	0.4937	6(0)	3.91	802	919	15.14	5.54
4	15	2.6	94.28	0.8381	1(0)	2.15	215	233	10.22	3.42
4	15	3.0	98.51	0.9560	0	–	14	14	3.11	2.15
4	30	1.0	8.19	0.0005	0	–	516	525	4.48	3.11
4	30	1.4	16.85	0.0048	7(0)	4.12	1235	1413	15.10	5.85
4	30	1.8	67.94	0.3136	5(1)	4.12	698	784	18.50	9.62
4	30	2.2	85.17	0.6178	7(1)	4.31	717	987	17.46	10.38
4	30	2.6	95.97	0.8837	0	–	130	138	8.84	6.46
4	30	3.0	98.75	0.9630	0	–	13	13	4.12	2.15
4	45	1.0	18.65	0.0065	22(5)	6.84	1632	2070	17.54	8.24
4	45	1.4	67.27	0.3044	14(3)	6.30	996	1246	20.43	10.32
4	45	1.8	84.26	0.5981	6(1)	4.31	632	801	16.75	7.99
4	45	2.2	93.46	0.8162	1(1)	2.71	286	307	8.43	4.12
4	45	2.6	97.71	0.9327	0	–	50	50	5.54	2.15
4	45	3.0	99.17	0.9752	0	–	12	12	3.68	2.15
4	60	1.0	88.09	0.6836	1(1)	2.71	309	367	13.70	7.99
4	60	1.4	93.28	0.8116	0	–	205	219	32.24	8.34
4	60	1.8	96.38	0.8952	0	–	106	109	8.71	4.93
4	60	2.2	98.19	0.9466	0	–	37	37	4.93	2.71

(continued on next page)

Table 1 (continued)

Impact speed (km s <sup>-1</sup> )	Impact angle (deg)	$\log(M_{\text{targ}}/M_{\text{imp}})$	Largest remnant diameter (km)	$M_{\text{Ir}}/M_{\text{targ}}$	Number of SMATS <sup>a</sup>	SMATS equivalent diameter (km)	Number of EEB primaries	Number of EEB secondaries	Largest EEB primary (km)	Largest EEB secondary (km)
4	60	2.6	99.10	0.9732	0	–	6	6	3.42	2.15
4	60	3.0	99.62	0.9886	0	–	1	1	2.15	2.15
4	75	0.6	98.82	0.9651	0	–	19	22	10.07	2.71
4	75	1.0	99.36	0.9807	0	–	8	9	46.26	4.64
4	75	1.4	99.64	0.9892	0	–	6	11	32.57	11.05
4	75	1.8	99.80	0.9941	0	–	6	8	11.98	8.24
4	75	2.2	99.87	0.9960	0	–	3	3	15.29	3.91
4	75	2.6	99.92	0.9975	0	–	5	5	2.15	2.15
4	75	3.0	99.97	0.9989	0	–	2	2	2.15	2.15
5	15	1.0	7.61	0.0004	0	–	40	40	4.93	2.71
5	15	1.4	7.78	0.0005	0	–	181	184	7.05	4.64
5	15	1.8	24.98	0.0156	16(2)	5.75	608	707	24.35	9.40
5	15	2.2	71.52	0.3657	8(1)	5.19	548	645	15.47	7.83
5	15	2.6	86.16	0.6397	0	–	905	1168	22.08	6.69
5	15	3.0	97.76	0.9341	0	–	32	34	3.91	2.71
5	30	1.0	6.62	0.0003	0	–	163	163	3.42	2.71
5	30	1.4	11.89	0.0017	2(0)	2.71	630	671	10.13	3.91
5	30	1.8	49.89	0.1242	61(7)	9.58	720	982	27.51	12.41
5	30	2.2	78.31	0.4803	3(1)	4.48	686	745	13.39	4.64
5	30	2.6	91.71	0.7712	17(3)	6.69	561	669	14.41	4.64
5	30	3.0	98.35	0.9513	0	–	30	30	4.12	2.71
5	45	1.0	12.30	0.0019	0	–	1183	1238	10.48	5.31
5	45	1.4	51.01	0.1327	62(14)	11.91	1125	1374	20.70	10.10
5	45	1.8	75.47	0.4298	2(0)	2.7	836	990	21.49	6.30
5	45	2.2	88.59	0.6952	15(5)	5.85	543	684	14.67	7.11
5	45	2.6	96.13	0.8882	0	–	131	139	6.77	2.71
5	45	3.0	98.90	0.9672	0	–	13	13	3.68	2.15
5	60	1.0	82.94	0.5705	6(2)	4.31	631	764	17.49	11.45
5	60	1.4	90.10	0.7315	6(0)	3.91	386	448	14.24	4.93
5	60	1.8	95.01	0.8576	1(0)	2.15	170	182	8.57	3.11
5	60	2.2	97.69	0.9322	0	–	50	51	4.79	2.71
5	60	2.6	98.84	0.9654	0	–	6	6	3.11	2.15
5	60	3.0	99.54	0.9863	0	–	2	2	2.15	2.15
5	75	1.0	99.39	0.9818	0	–	6	32	43.94	5.07
5	75	1.4	99.73	0.9919	0	–	1	1	4.31	2.15
5	75	1.8	99.84	0.9951	0	–	6	6	22.15	3.11
5	75	2.2	99.88	0.9963	0	–	12	15	12.82	2.71
5	75	2.6	99.91	0.9973	0	–	1	1	2.15	2.15
5	75	3.0	99.96	0.9986	0	–	1	1	2.15	2.15
6	15	1.0	6.54	0.0003	0	–	13	13	2.71	2.15
6	15	1.4	7.94	0.0005	0	–	84	84	4.64	2.71
6	15	1.8	21.30	0.0097	6(2)	5.31	276	336	18.06	6.91
6	15	2.2	65.49	0.2809	0	–	512	638	16.02	9.55
6	15	2.6	82.75	0.5665	2(0)	2.71	606	629	6.84	3.42
6	15	3.0	95.73	0.8771	0	–	202	215	3.68	2.71
6	30	1.0	7.05	0.0003	0	–	70	70	3.42	3.11
6	30	1.4	9.13	0.0008	0	–	265	268	8.34	3.11
6	30	1.8	27.62	0.0211	55(17)	10.13	781	969	21.07	10.83
6	30	2.2	73.36	0.3948	8(2)	4.79	478	542	20.08	5.65
6	30	2.6	85.70	0.6294	0	–	885	1099	12.54	6.38
6	30	3.0	97.20	0.9183	0	–	115	119	4.79	2.71
6	45	1.0	10.39	0.0011	1(0)	2.15	550	565	9.58	4.12
6	45	1.4	27.46	0.0207	13(4)	5.54	1106	1343	22.23	7.66
6	45	1.8	66.64	0.2959	39(14)	10.32	665	823	22.82	8.14
6	45	2.2	83.03	0.5723	2(0)	2.71	808	934	19.99	6.84
6	45	2.6	93.56	0.8188	4(0)	3.42	369	440	9.40	3.91
6	45	3.0	98.45	0.9543	0	–	37	37	3.42	2.15
6	60	1.0	76.61	0.4496	6(0)	3.91	851	961	39.49	9.55
6	60	1.4	86.58	0.6490	7(2)	4.48	672	770	15.86	5.54
6	60	1.8	93.03	0.8050	0	–	312	356	10.89	4.12

(continued on next page)

Table 1 (continued)

Impact speed (km s <sup>-1</sup> )	Impact angle (deg)	$\log(M_{\text{targ}}/M_{\text{imp}})$	Largest remnant diameter (km)	$M_{\text{Ir}}/M_{\text{targ}}$	Number of SMATS <sup>a</sup>	SMATS equivalent diameter (km)	Number of EEB primaries	Number of EEB secondaries	Largest EEB primary (km)	Largest EEB secondary (km)
6	60	2.2	96.94	0.9110	0	–	101	105	7.55	3.11
6	60	2.6	98.72	0.9621	0	–	17	18	4.12	2.15
6	60	3.0	99.45	0.9835	0	–	3	3	3.11	2.15
6	75	1.0	99.44	0.9831	0	–	11	34	46.03	3.42
6	75	1.4	99.70	0.9909	0	–	11	28	31.05	7.49
6	75	1.8	99.82	0.9944	0	–	3	3	23.48	2.71
6	75	2.2	99.86	0.9957	0	–	27	29	7.48	3.42
6	75	2.6	99.90	0.9971	0	–	2	2	2.15	2.15
6	75	3.0	99.95	0.9983	0	–	0	0	–	–
7	15	1.4	6.77	0.0003	0	–	41	41	3.91	2.15
7	15	1.8	17.64	0.0055	3(1)	3.68	151	158	15.41	3.68
7	15	2.2	58.53	0.2005	3(0)	3.11	526	679	16.44	9.44
7	15	2.6	79.75	0.5071	0	–	475	494	7.99	4.64
7	15	3.0	89.95	0.7276	48(8)	8.66	628	1083	33.62	5.94
7	30	1.0	6.84	0.0003	0	–	24	24	4.12	2.15
7	30	1.4	10.80	0.0013	1(0)	2.15	81	81	4.64	3.42
7	30	1.8	17.73	0.0056	6(3)	4.93	515	588	17.46	6.30
7	30	2.2	65.22	0.2774	5(3)	5.19	554	655	19.65	8.14
7	30	2.6	82.44	0.5603	1(0)	2.15	653	675	9.44	4.48
7	30	3.0	94.58	0.8459	6(0)	3.9	392	435	4.31	3.42
7	40	2.6	85.80	0.6316	1(0)	2.15	844	1035	11.82	6.77
7	45	1.0	9.86	0.0010	2(0)	2.71	299	306	6.54	3.91
7	45	1.4	19.19	0.0071	3(0)	3.11	724	831	17.27	4.79
7	45	1.8	58.82	0.2035	11(2)	5.07	741	910	21.28	6.13
7	45	2.2	78.53	0.4843	0	–	599	675	18.33	7.66
7	45	2.4	84.02	0.5930	1(0)	2.15	768	854	17.39	4.12
7	45	2.6	88.71	0.6981	119(14)	11.21	632	974	13.59	8.62
7	45	2.8	94.50	0.8438	1(0)	2.15	327	378	6.30	3.42
7	45	3.0	97.51	0.9272	0	–	103	107	3.68	3.11
7	50	2.6	93.21	0.8098	10(1)	4.79	405	452	12.43	4.64
7	60	1.0	70.54	0.3510	5(0)	3.6	782	947	39.19	6.98
7	60	1.4	82.04	0.5520	4(1)	3.91	846	994	17.49	6.04
7	60	1.8	90.22	0.7343	0	–	545	648	14.41	6.30
7	60	2.2	95.32	0.8659	1(0)	2.15	223	231	7.18	3.11
7	60	2.6	98.38	0.9522	0	–	36	37	3.42	2.71
7	60	3.0	99.32	0.9796	0	–	4	4	2.15	2.15
7	75	1.0	99.43	0.9829	0	–	18	62	35.14	5.19
7	75	1.4	99.68	0.9905	0	–	2	14	30.68	3.42
7	75	1.8	99.82	0.9945	0	–	2	2	2.15	2.15
7	75	2.2	99.85	0.9955	0	–	26	28	6.76	2.15
7	75	2.6	99.92	0.9975	0	–	1	1	2.15	2.15
7	75	3.0	99.94	0.9980	0	–	0	0	–	–

<sup>a</sup> The total number of all SMATS particles is listed first, followed by the number of SMATS particles larger than the single-particle resolution limit in parentheses.

changed by (i) particle–particle interactions and by (ii) the  $\Delta V$  of material reaccreting onto the remaining target body. Together, these effects allow some impact debris to enter into orbit around the remaining target body, which is a gravitationally reaccreted rubble pile.<sup>3</sup> We refer to this type of satellite as a SMATS (SMASHed Target Satellite). We also

find that numerous smaller fragments escaping the impact site have similar trajectories, such that many become bound to one another. We refer to this type of satellite as an EEB (Escaping Ejecta Binary). Figure 1 illustrates these two types of satellite systems.

### 3.1. SMATS

Since most SMATS debris will eventually either reaccrete onto the primary or accrete with other SMATS debris while in orbit, the total number (mass) of SMATS particles remaining in orbit about the largest remnant at the end of our 4-day  $N$ -body simulations may be crudely related to the

<sup>3</sup> Strictly speaking, the resulting largest remnants generated in our simulations are not rubble piles, since we impose particle merging during the gravitational reaccumulation phase. Conceptually, however, the largest remnants are bodies that have been completely shattered and reassembled, a special case of a gravitational aggregate fitting one definition of a rubble pile (see Richardson et al., 2002, for a review).

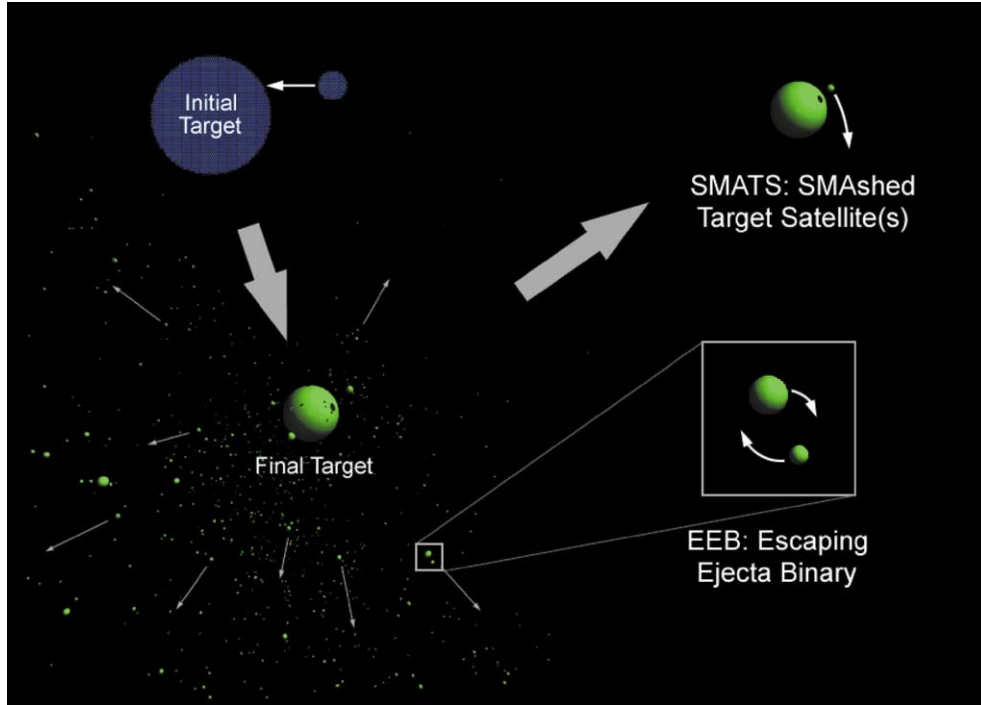


Fig. 1. Two classes of satellites resulting from large impacts between asteroids. SMashed Target Satellites (SMATS) form from impact debris that enters into orbit around the remaining target body, which is a gravitationally reaccreted rubble pile. Escaping Ejecta Binaries (EEBs) result when smaller fragments escaping the impact site have similar trajectories, such that they become gravitationally bound to one another.

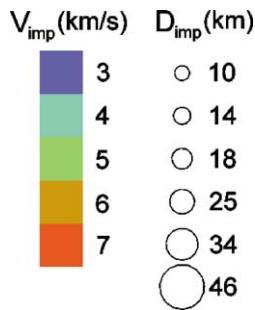


Fig. 2. Key to symbol colors and sizes for Figs. 3–6. Dot colors are coded according to impactor speed and dot sizes are coded according to impactor diameter.

eventual size of the single SMATS satellite that will likely remain in orbit about the largest remnant. To be conservative, we exclude from our analysis those particles with periapsis less than  $2R_{Ir}$  (particles very near an irregularly-shaped primary may be likely to reimpact the primary and our model does not account for irregularly-shaped primaries; see Scheeres et al. (2002) for a more detailed discussion), and particles that pass beyond the Hill sphere of the largest remnant, assuming a heliocentric distance of 3 AU (satellites that approach a primary’s Hill sphere are probably unstable; Hamilton and Krivov, 1997). Figure 3 shows the resulting equivalent SMATS diameters as a function of the diameter of the largest remnant (a key to symbol colors and sizes is shown in Fig. 2). In this figure, sub-catastrophic (low energy) impacts are represented to the far right and super-catastrophic (high energy) to the far left. It appears that the

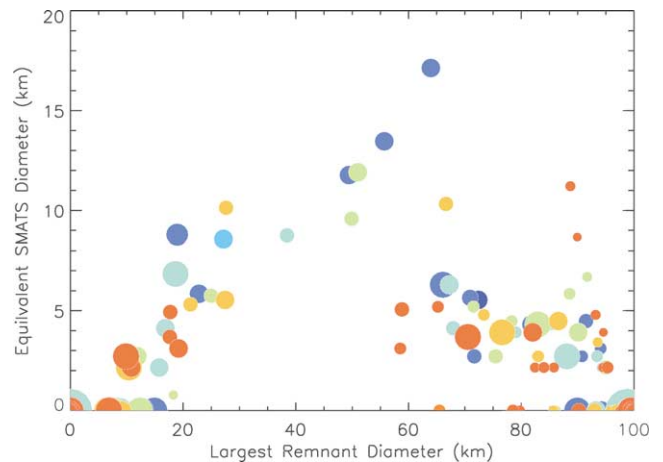


Fig. 3. Equivalent SMATS diameter versus the diameter of the largest remnant.

largest SMATS are formed around the largest remnants of moderately catastrophic impacts, in which the mass of the largest remnant is less than half that of the original target. For our 100-km diameter targets this translates to those largest remnant diameters of  $\sim 80$  km or less. The three large blue dots near the peak in equivalent SMATS diameter in Fig. 3 represent impacts of 34-km diameter projectiles at  $3 \text{ km s}^{-1}$  at impact angles of  $25^\circ$ – $35^\circ$ . Such impacts appear very efficient at producing relatively large satellites around the largest remnant. We find that for a given value of  $M_{Ir}/M_{targ}$  similar numbers of SMATS are produced independent of impact angle, at least up through  $45^\circ$  and possibly

up through  $60^\circ$ . No SMATS were produced in any of the simulations with impact angles of  $75^\circ$ , all of which resulted in very large values of  $M_{lr}/M_{targ}$  (well over 0.9). In these highly oblique impacts the top of the target asteroid is simply “shaved off,” the target is not disrupted, and little if any debris remains in stable orbit around the remnant.

At lower impact energies the events are essentially large cratering impacts and most ejected material either accretes into a small satellite or eventually reaccretes onto our spherical remnants, leaving little orbiting material. Figure 4 shows the primary-to-secondary diameter ratio of the SMATS systems resulting from our simulations. The right portion of the figure, for largest remnants larger than about 80 km in diameter, represents the results of large cratering events. A trend toward larger diameter ratios (smaller satellites) for smaller-scale impacts is evident. For comparison, the Ida–Dactyl system has a primary to secondary diameter ratio of  $\sim 22$ . The shaded portion of Fig. 4 indicates those diameter ratios (greater than  $\sim 25$ ) that are beyond the detection capabilities of existing ground-based adaptive optics search programs for separations typical of SMATS (e.g., Merline et al., 2002a). The significant number of SMATS systems resulting from cratering impacts (see also Durda and Geissler, 1996) that lie to the right and above this limit, and because there are many more cratering collisions than catastrophic collisions (because of the steep size distribution of impactors), suggests that a large number of Ida–Dactyl-like satellite systems remain undetected in the main asteroid belt. It should be noted, however, that the smallest satellites at the upper right portion of Fig. 4 are near or at the SPH resolution limits of our simulations, so details in that portion of the figure should be treated with appropriate caution.

At very high impact energies targets are severely disrupted, resulting in small largest remnant sizes and less bound debris.

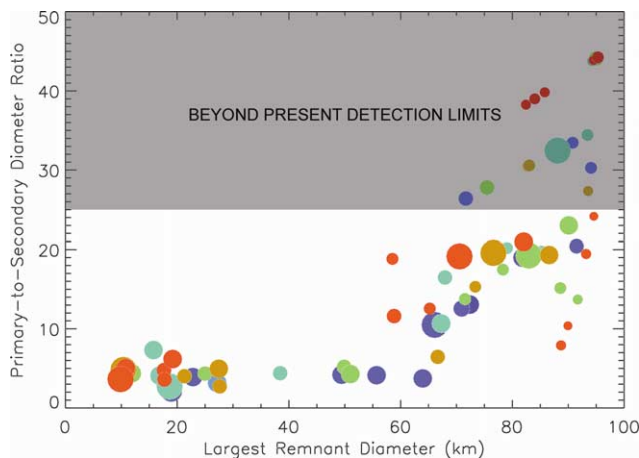


Fig. 4. Primary-to-secondary diameter ratio of SMATS systems versus the diameter of the largest remnant. The shaded region indicates the current observational limits for typical SMATS systems, namely main-belt companions separated by about 0.5 arcsec. Recently, however, a SMATS system has been detected having a brightness difference of 8.5 magnitudes (diameter ratio about 50), but at larger separations (see Merline et al., 2003b).

### 3.2. EEBs

Figure 5 shows the number of EEBs as a function of the diameter of the largest remnant. As was true for SMATS, it appears that most EEBs result from moderately catastrophic impacts, although many are also produced by the highly disruptive impacts resulting from large projectiles striking at or below the average main-belt mutual impact speed of  $\sim 5 \text{ km s}^{-1}$ . Other large impactors striking at higher speeds evidently eject collision debris so energetically that few escaping fragments can remain bound to each other. The three large blue dots near the peak in the number of EEBs in Fig. 5 are the same three near the peak in the diameter of SMATS in Fig. 3. Such large-scale, low-speed, slightly off-center impacts appear very efficient at producing large numbers of modest-size binaries among their escaping ejecta in addition to large SMATS.

Since the diameter of the largest remnant is related to the total disruptive energy imparted to the original target, Fig. 5 can be recast in terms of the impactor kinetic energy (Fig. 6). Looking at the simulation results grouped by impact angle (the 5 panels of Fig. 6), some interesting trends are readily apparent. The number of EEB primaries appears to be a rather well-defined function of the impactor kinetic energy and impact angle, with little scatter around the general trend for all but the most oblique impacts. For all impact angles few EEBs are produced at the lowest impactor kinetic energies, as might be expected: such collisions result in little more than large cratering events and little material escapes the target asteroid. As impactor kinetic energy increases, more energy is available to fragment the target and eject significant numbers of debris fragments on escaping trajectories, so more EEB systems are produced. For impact angles less than about  $45^\circ$ , there appears to be an optimal amount of impactor kinetic energy ( $\sim 10^{23}$ – $10^{24}$  J, corresponding to a specific impact energy of  $\sim 7 \times 10^4$ – $7 \times 10^5 \text{ J kg}^{-1}$ ) to produce the largest number of EEB systems. Note again that the largest numbers of EEBs are formed by large-scale, low-

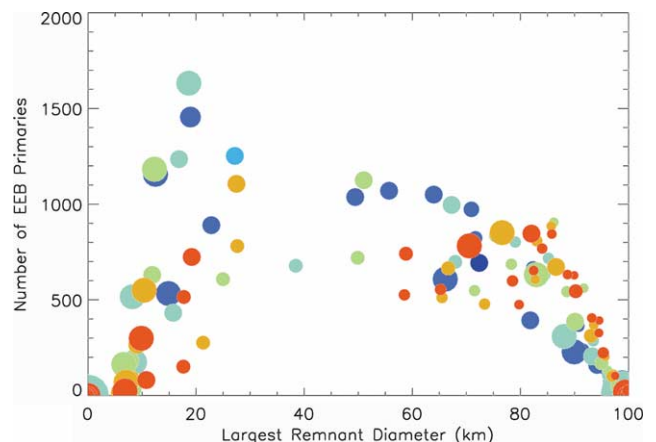


Fig. 5. Number of EEB primaries versus the diameter of the largest remnant.

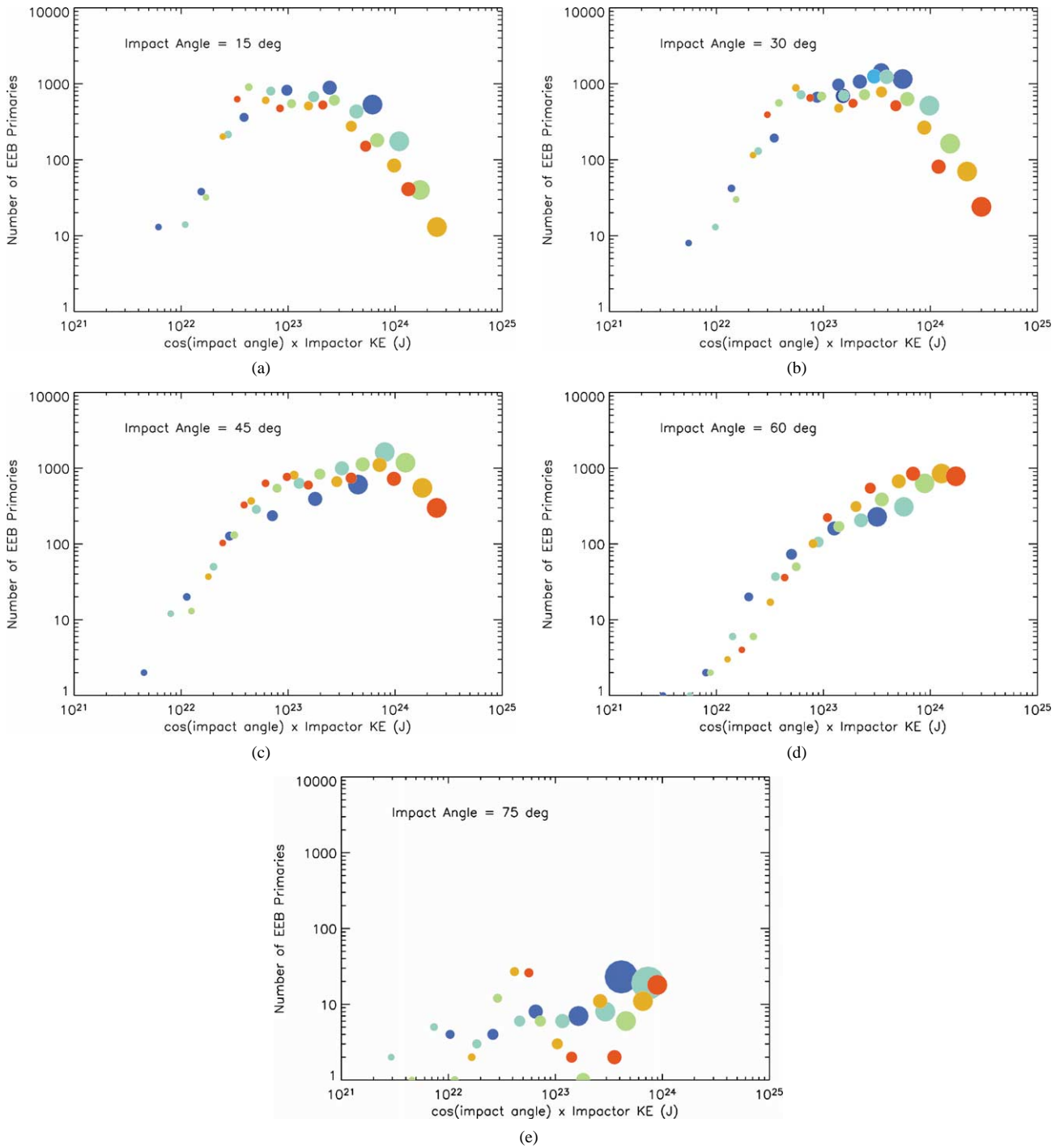


Fig. 6. (a) Number of EEB primaries versus impactor kinetic energy for those simulations with an impact angle of  $15^\circ$ . In order to ‘normalize’ the energy imparted to the target by an oblique impact relative to that imparted by a normal-incidence impact, we multiply the impactor kinetic energy by the cosine of the impact angle. (b) Same as (a), but for those simulations with an impact angle of  $30^\circ$ . (c) Same as (a), but for those simulations with an impact angle of  $45^\circ$ . (d) Same as (a), but for those simulations with an impact angle of  $60^\circ$ . (e) Same as (a), but for those simulations with an impact angle of  $75^\circ$ .

speed impacts with impact angles near  $30^\circ$ . At still higher impact energies, the number of EEBs decreases, suggesting that the targets are so violently shattered and dispersed that few debris fragments can remain bound to each other to form stable orbiting pairs. For impact angles larger than about  $45^\circ$ , no such decrease in the number of EEBs is observed for the highest impact energies. At these more oblique im-

pect angles the impactor kinetic energy is not as strongly coupled into the target, resulting in less target disruption. Also, significant numbers of debris fragments are ‘sprayed off’ the target in something like a collimated ‘jet,’ rather than being dispersed with high energy in all directions, so that large numbers of EEB systems are still able to form. In the most oblique impacts, the well-defined functional depen-

dence of the number of EEBs with impactor kinetic energy breaks down. Little material is removed from the target and fewer EEBs are produced overall.

### 3.3. An in-depth look at a single simulation outcome

Our numerical procedure yields a wealth of data for each test case, perhaps more than can be easily communicated in a single paper. For that reason, we concentrate in this section on the results from a single simulation that generates both SMATS and EEBs, as an example of the information that remains to be mined from the simulation data set. We chose to examine here the simulation of a 34-km diameter impactor striking a 100-km diameter target at  $3 \text{ km s}^{-1}$  at an impact angle of  $30^\circ$  (i.e., the most efficient SMATS- and EEB-forming scenario; see the peak in Fig. 6b). In terms of the parameters shown in Table 1,  $\log(M_{\text{targ}}/M_{\text{imp}}) = 1.4$ . The largest remnant left over from the collision has a diameter of 55.7 km and a mass of  $2.44 \times 10^{17} \text{ kg}$ .

After 4 days of post-impact simulation time, we found 92 SMATS attained stable orbits. The semimajor axis and orbital eccentricity distributions of these bodies around the largest remnant are shown in Figs. 7 and 8. To be conservative, particles with a periaapse distance smaller than twice the radius of the largest remnant are assumed to be unstable and are not plotted, though our integration routines continue to track their behavior in the simulation.

Nearly half ( $\sim 43\%$ ) of the SMATS in this run have semimajor axes (Fig. 7) less than  $\sim 20$  times the radius of the largest remnant,  $R_{\text{lr}}$ , and most of those have semimajor axes in the range  $\sim 4\text{--}7R_{\text{lr}}$ , consistent with the observed semimajor axes  $a$  of observed satellite systems in the main belt. A small fraction of SMATS have significantly larger  $a$  values, with one particular SMATS nearly reaching the brink of the largest remnant's Hill sphere. Most SMATS are on highly eccentric orbits, with many having  $e > 0.8$ . Because the orbits of most SMATS cross one another, we expect them to

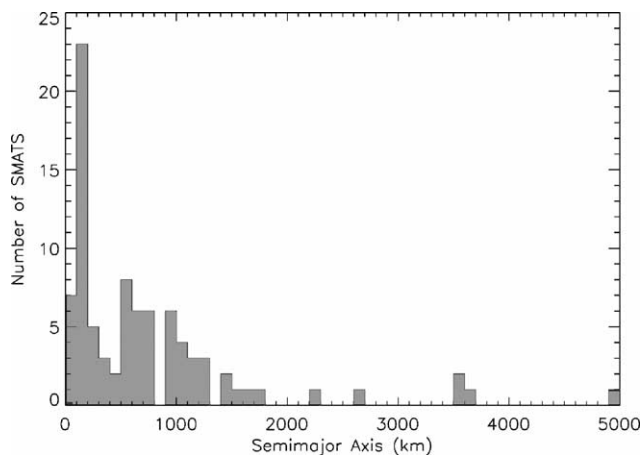


Fig. 7. Distribution of semimajor axes for the SMATS particles formed in the case of a 34-km diameter impactor striking a 100-km diameter target at  $3 \text{ km s}^{-1}$  at an impact angle of  $30^\circ$ . Four SMATS particles lie off scale to the right, with semimajor axes of 6245, 6467, 6652, and 12,744 km.

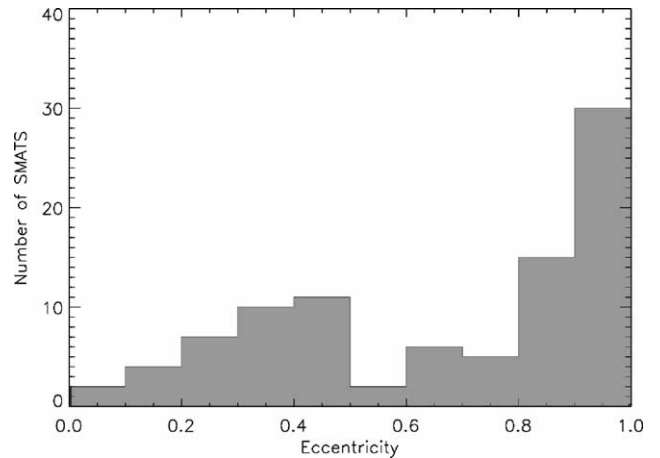


Fig. 8. Distribution of orbital eccentricities for the SMATS particles formed in the case of a 34-km diameter impactor striking a 100-km diameter target at  $3 \text{ km s}^{-1}$  at an impact angle of  $30^\circ$ .

eventually collide with one another and accrete into a single large SMATS orbiting close to the primary (i.e.,  $a <$  several  $R_{\text{lr}}$ ). In this particular case, the diameter of the resulting SMATS would be 13.46 km, such that the ratio of the diameter of the largest remnant (i.e., the primary) to the resulting SMATS (i.e., the secondary) is  $\sim 4$ . Note that we do not model the further dynamical evolution of these particles because:

- (i) the largest remnant in each run is defined to be a sphere, such that our models would miss gravitational perturbations produced by realistic asteroid shapes;
- (ii) our code does not currently include the effects of mutual tidal forces;
- (iii) the code has not yet been optimized for this task.

We save this interesting problem for future work.

The same simulation produced 1070 EEBs. Many of these EEB systems involve more than two particles; we find there are 1406 secondaries after 4 days of post-impact simulation time, down from  $\sim 1600$  immediately after the breakup event. About half of the EEB systems consist of equal-size components at the resolution limit of the simulations. The rest are systems with secondary-to-primary mass ratio less than 1 (Fig. 9). For this run, the diameter of the largest EEB primary is 29.2 km and the diameter of the largest EEB secondary (which in this case was not orbiting the largest primary) is 9.04 km. These values are approaching the small-size primaries in wide binaries recently found in the main belt (see Section 3.4).

The distribution of the semimajor axes of the secondaries' orbits with respect to the primaries for the EEBs is shown in Fig. 10. We find that the average EEB semimajor axis is  $\sim 80 \text{ km}$  after 4 days of simulation time, very similar to the average value found immediately after the impact. Some EEBs, however, have much more extended orbits. Figure 11 shows the orbital eccentricity distribution (again, of

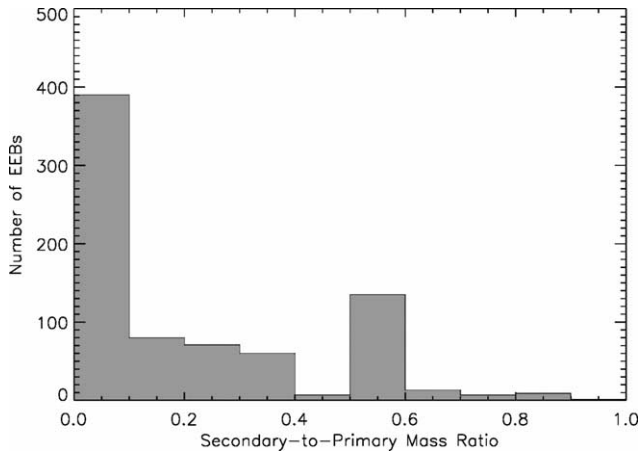


Fig. 9. Secondary-to-primary mass ratio for the EEBs formed in the case of a 34-km diameter impactor striking a 100-km diameter target at  $3 \text{ km s}^{-1}$  at an impact angle of  $30^\circ$ . Not plotted are 633 EEBs with secondary-to-primary mass ratio equal to 1 (i.e., individual particles orbiting other individual particles at the resolution limit of the simulation).

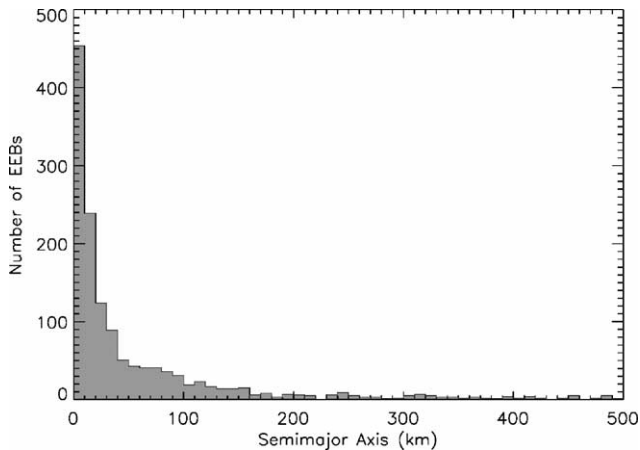


Fig. 10. Distribution of semimajor axes for the EEBs formed in the case of a 34-km diameter impactor striking a 100-km diameter target at  $3 \text{ km s}^{-1}$  at an impact angle of  $30^\circ$ .

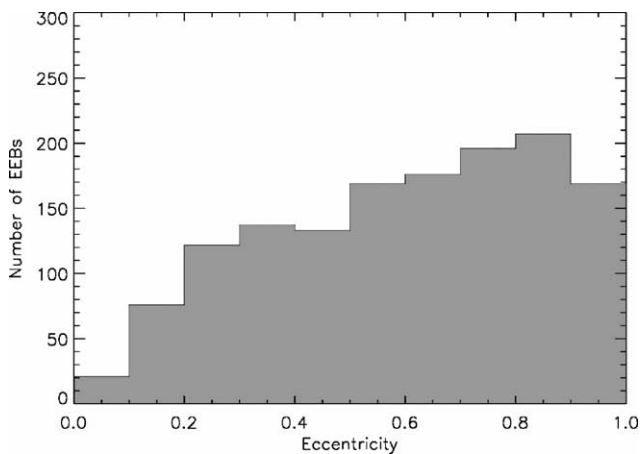


Fig. 11. Distribution of orbital eccentricities for the EEBs formed in the case of a 34-km diameter impactor striking a 100-km diameter target at  $3 \text{ km s}^{-1}$  at an impact angle of  $30^\circ$ .

the secondaries' orbits with respect to the primaries) of the EEBs, which peaks near  $e \approx 0.85$  and has an average value of  $\sim 0.6$ . Note that all these values should be treated with some caution, given that our EEB primaries and secondaries are modeled as simple spherical bodies that do not produce tidal forces, which will tend to alter their initial orbits.

Durda (1996) presented results from a simple empirical model that suggested that EEB-like binary pairs might originate as radially-oriented particles within the original target body, although it was pointed out that this might be an artifact of the simple model. Dorissoundiram et al. (1997) conducted similar modeling with a more sophisticated, though still largely empirical, model of the initial fragment ejection velocities and did not see such an effect. Our new models allow us to map out, for both SMATS and EEBs separately, the distribution within the target asteroid of the original locations of those SPH particles which eventually end up in bound satellite systems (Fig. 12). Although the individual components of specific EEB pairs are not highlighted here, we see no generally apparent radial orientation of EEB particles within the target, suggesting that the radial alignment noted in Durda (1996) was indeed likely a model artifact. As might be expected, few if any particles from near the impact site in the upper right portion of the plotted target are found to have ended up in bound satellite systems—material from this region was either vaporized or ejected at relative speeds so great as to preclude mutual capture into bound pairs. A few EEB particles originated in the impactor; the end of the SPH simulation for this case shows some apparently intact fragments from the rear of the impactor moving away to the upper left.

### 3.4. Comparison with observed main-belt satellite systems

Work by Weidenschilling et al. (1989), and updated in Merline et al. (2002a), indicates that there should be observable characteristic differences between satellite systems formed by the SMATS vs. the EEBs mechanisms. Specifically, based on theoretical energetics and angular momentum arguments, SMATS would be expected to show large size ratios and have small orbital separations, while EEBs should have less bias toward large size ratios and could be formed much further from the primary.

Until recently, most main-belt satellite systems (90 Antiope being an exception; Merline et al., 2000) had similar size ratios (about 10–25), and similar orbital separations (in terms of primary radii, roughly 10) (Merline et al., 2002a). But two recently-discovered binaries are different. They show size ratios of 3–4 and have orbital separations of at least  $23R_p$  in one case and  $100R_p$  in another (Merline et al., 2002b; Merline et al., 2003a).

According to Weidenschilling et al.'s (1989) estimates, the timescale for tidal evolution of these two new systems from close-in orbits originating from a SMATS impact, to their present wide orbits, would be far longer than any reasonable age. Thus, it is likely that these new systems, (3749)

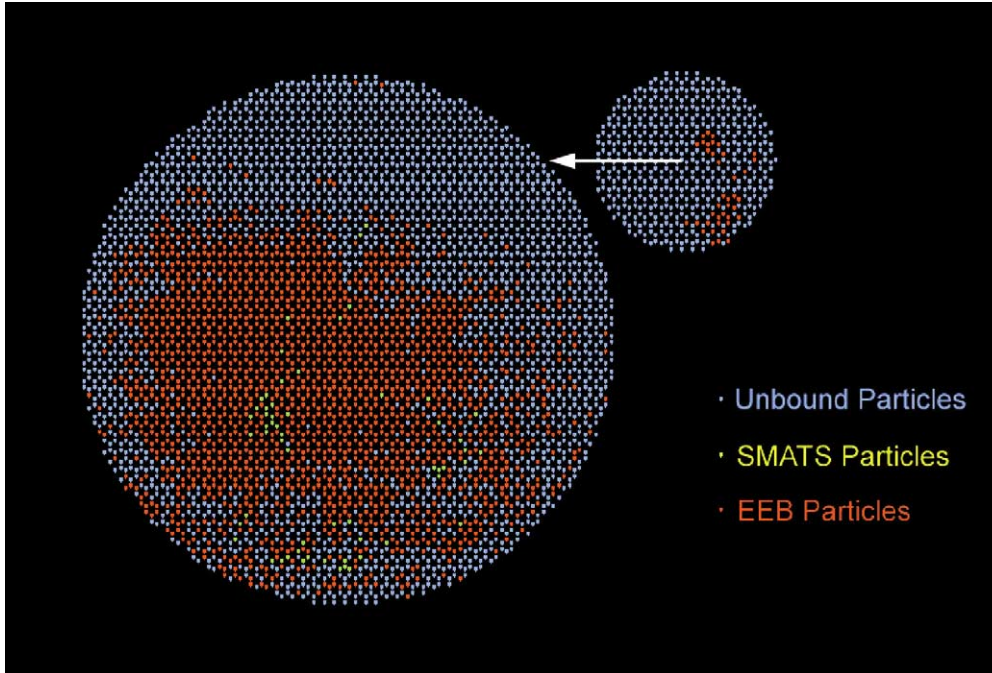


Fig. 12. The locations within the target body (in the case of a 34-km diameter impactor striking a 100-km diameter target at  $3 \text{ km s}^{-1}$  at an impact angle of  $30^\circ$ ) from which those SPH particles that end up in satellite pairs originated. Those particles not ending up in bound satellite systems are shown in blue; particles ending up as SMATS are shown in yellow; particles ending up as EEBs are shown in red. This is a 'transparent' view through the target looking along the  $z$ -axis: the large concentration of EEB particles near the central region of the target in this view indeed lie largely near the core of the target and not in an outer 'shell' surrounding the core.

Balam and (1509) Esclangona, are likely the first observed examples of binaries produced by the EEB mechanism (Merline et al., 2002b).

The numerical simulations described here can produce satellite systems wholly consistent with those observed in the main belt. Size ratios of SMATS (Fig. 4) in the range 10–25 are common, while EEBs (Fig. 9) are clearly more biased toward smaller size ratios than the SMATS (i.e., the components are more similar in size).

### 3.5. The frequency of SMATS-forming impacts

One of the interesting implications from our work is that many different kinds of collisions produce SMATS and EEBs. Using our numerical results, we can compute the frequency of satellite-forming events in the current main belt and compare those results with data from asteroid satellite surveys. We start our analysis by examining the frequency of SMATS-forming impacts. Merline et al. (2001), after a survey of 300 main belt asteroids, reported that 5 asteroids with  $D > 140 \text{ km}$  had relatively large satellites (i.e., a few tens of kilometers in diameter). One of these SMATS, (90) Antiope, is apparently associated with the catastrophic disruption of the Themis parent body. The remaining SMATS, (22) Kalliope, (45) Eugenia, (87) Sylvia, and (762) Pulcova, have primary-to-secondary diameter ratios smaller than 25. Detection limits of present ground-based adaptive optics searches limits the discovery of SMATS to primary-

to-secondary diameter ratios smaller than 25 (e.g., Merline et al., 2002a).

None of the primaries described above other than (90) Antiope and possibly (87) Sylvia are associated with any prominent concentration of asteroids that could be considered an asteroid family (D. Nesvorný, 2003, personal communication). Nesvorný's search was performed on a proper element database containing approximately 70,000 main-belt asteroids (Milani and Knežević, 1994; Knežević et al., 2002). We point out that this proper element database was large enough to uncover the Karin cluster, a cluster of asteroids produced by the breakup of a  $\sim 25$ -km diameter asteroid 5.8 Myr ago (Nesvorný et al., 2002), and several additional asteroid clusters that are also believed to be by-products of recent disruption events (Nesvorný et al., 2003). Thus, if the SMATS formation scenario described by this paper is correct, and if the SMATS associated with (22) Kalliope, (45) Eugenia, (87) Sylvia, and (762) Pulcova were not produced in some primordial epoch, the non-family SMATS must have been produced by non-catastrophic collisions.

Based on this hypothesis, we can compute the rate of SMATS-forming events by non-catastrophic collisions in the present-day main belt. The equation to compute this value is:

$$\text{Rate} = P_i \cdot (D_{\text{targ}}/2)^2 \cdot N(D_{\text{min}} < D < D_{\text{max}}) \cdot \text{Prob}(\theta) \cdot \text{Prob}(V).$$

The value  $P_i = 2.85 \times 10^{-18} \text{ km}^{-2} \text{ yr}^{-1}$ , the intrinsic collision probability of asteroids striking other asteroids in

the main belt (Farinella and Davis, 1992; Bottke et al., 1994). We choose  $D_{\text{targ}} = 140$  km, the diameter of the smallest SMATS primaries observed to date. The number of available impactors over a given size range,  $N(D_{\text{min}} < D < D_{\text{max}})$ , can be found from the values reported by Jedicke and Metcalfe (1998) (see also Durda et al., 1998; Jedicke et al., 2002). The size range chosen in our model is given by the  $\log(M_{\text{targ}}/M_{\text{imp}})$  spacing listed in Table 1. The value  $\text{Prob}(\theta)$  is the probability that an asteroid will strike the target at a given impact angle  $\theta$  (see Section 3); this probability is represented by a  $\sin^2(\theta)$  function (Shoemaker, 1962). The value  $\text{Prob}(V)$  is the probability that our projectile will strike our target asteroid at a given impact speed  $V$ . Using the impact speed distribution reported in Bottke et al. (1994), we find that

$$\begin{aligned}\text{Prob}(V < 3.5 \text{ km s}^{-1}) &= 0.25, \\ \text{Prob}(3.5 < V < 4.5 \text{ km s}^{-1}) &= 0.18, \\ \text{Prob}(4.5 < V < 5.5 \text{ km s}^{-1}) &= 0.17, \\ \text{Prob}(5.5 < V < 6.5 \text{ km s}^{-1}) &= 0.14, \quad \text{and} \\ \text{Prob}(V > 6.5 \text{ km s}^{-1}) &= 0.26.\end{aligned}$$

Putting these values together, we find that the frequency of SMATS-forming events by non-catastrophic collisions in the present-day main belt is  $1.73 \times 10^{-11} \text{ yr}^{-1}$ , where we include all collisions where the diameter of the largest remnant is 80% the diameter of the original body (i.e., a barely-catastrophic disruption), to  $8.8 \times 10^{-12} \text{ yr}^{-1}$ , where we include all collisions where the diameter of the largest remnant is 90% the diameter of the original body (i.e., sub-catastrophic disruption). If we assume that the main belt has not changed a great deal over the last 4 Gyr, and that the number of  $D > 140$  km targets today (94) is roughly the same number that existed 4 Gyr ago, we expect these production rates to produce 3–6 SMATS. These results appear to be an excellent match with the 4 non-family SMATS found to date. They also give us increased confidence that our numerical technique, despite its many approximations, is producing reasonable results.

An interesting aspect of our results is that the number of SMATS orbiting  $D > 140$  km asteroids appears consistent with normal collisional evolution over the last 4 Gyr. Recent work has shown, however, that collisions in the primordial main belt (i.e., from 4.56 to possibly 4.4 Gyr ago) were much more numerous than in today's main belt (Bottke et al., 2003). Assuming that collisional outcomes in the primordial main belt were similar to those occurring today, Bottke et al.'s (2003) results imply that many large asteroids should have SMATS. This raises the question: What happened to all of the putative SMATS? One possibility is that SMATS collisional disruption events in the primordial main belt dominated SMATS formation events. If true, perhaps SMATS can only survive in a more quiescent, low-mass main belt. Another possibility is that the dynamical excitation event that removed 99% of the bodies from the primor-

dial main belt (e.g., Petit, 2001, 2002) also stripped most primaries of their SMATS. Hence, SMATS formed in the primordial epoch were “erased” by the dynamical excitation event, leaving behind a tabula rosa where non-catastrophic collisions could leave their mark over the last 4.4–4.5 Gyr of Solar System history. If true, the paucity of SMATS found around large asteroids today provide strong constraints on the nature of the mechanisms that caused the dynamical excitation event some 4.4–4.5 Gyr ago.

## Acknowledgments

We thank Patrick Michel and Sarah Stewart-Mukhopadhyay for their very helpful reviews. This work was supported by the National Science Foundation Planetary Astronomy Program, Grant 0098484, the NASA Planetary Geology and Geophysics Program, Grant NAG5-8914, and the NASA Origins of Solar Systems Program, Grant NAG5-11722. Numerical simulations were assisted by support from NASA's Intelligent Systems Program though subcontract from JPL; we thank especially D. Mazzoni and D. DeCoste. We thank Peter Tamblyn for his assistance in producing Fig. 12.

## References

- Anderson, J.L.B., Schultz, P.H., Heineck, J.T., 2002. Evolving flow-field centers in oblique impacts. In: Proc. Lunar Planet. Conf. Sci. 33rd. Abstract 1762.
- Asphaug, E., 1997. Impact origin of the Vesta family. *Meteorit. Planet. Sci.* 32, 965–980.
- Asphaug, E., Melosh, H.J., 1993. The Stickney impact of Phobos: a dynamical model. *Icarus* 101, 144–164.
- Asphaug, E., Ryan, E.V., Zuber, M.T., 2003. Asteroid interiors. In: Bottke, W.F., Cellino, A., Paolicchi, P., Binzel, R.P. (Eds.), *Asteroids III*. Univ. of Arizona Press, Tucson, pp. 463–484.
- Barnes, J., Hut, P., 1986. A hierarchical  $O(N \log N)$  force-calculation algorithm. *Nature* 324, 446–449.
- Benz, W., Asphaug, E., 1994. Impact simulations with fracture: I. Method and tests. *Icarus* 107, 98–116.
- Benz, W., Asphaug, E., 1995. Simulations of brittle solids using smooth particle hydrodynamics. *Comput. Phys. Commun.* 87, 253–265.
- Benz, W., Asphaug, E., 1999. Catastrophic disruptions revisited. *Icarus* 142, 5–20.
- Bottke Jr., W.F., Melosh, H.J., 1996a. The formation of asteroid satellites and doublet craters by planetary tidal forces. *Nature* 381, 51–53.
- Bottke Jr., W.F., Melosh, H.J., 1996b. The formation of binary asteroids and doublet craters. *Icarus* 124, 372–391.
- Bottke Jr., W.F., Nolan, M.C., Greenberg, R., Kolvoord, R.A., 1994. Velocity distributions among colliding asteroids. *Icarus* 107, 255–268.
- Bottke, W., Durda, D., Nesvorný, D., Jedicke, R., 2003. The fossilized size distribution of the main asteroid belt. In: 6th Workshop on Catastrophic Disruption in the Solar System. Abstract.
- Canup, R.M., Asphaug, E., 2001. The lunar-forming giant impact. *Nature* 412, 708–712.
- Davis, D.R., Chapman, C.R., Greenberg, R., Weidenschilling, S.J., Harris, A., 1979. Collisional evolution of asteroids: populations, rotations, and velocities. In: Gehrels, T. (Ed.), *Asteroids*. Univ. of Arizona Press, Tucson, pp. 528–557.
- Davis, D.R., Chapman, C.R., Weidenschilling, S.J., Greenberg, R., 1985. Collisional history of asteroids: evidence from Vesta and the Hirayama families. *Icarus* 62, 30–53.

- Davis, D.R., Weidenschilling, S.J., Farinella, P., Paolicchi, P., Binzel, R.P., 1989. Asteroid collisional evolution: effects on sizes and spins. In: Binzel, R.P., Gehrels, T., Matthews, M.S. (Eds.), *Asteroids II*. Univ. of Arizona Press, Tucson, pp. 805–826.
- Dorissoundiram, A., Paolicchi, P., Verlicchi, A., Cellino, A., 1997. The formation of binary asteroids as outcomes of catastrophic collisions. *Planet. Space Sci.* 45, 757–770.
- Durda, D.D., 1996. The formation of asteroidal satellites in catastrophic collisions. *Icarus* 120, 212–219.
- Durda, D.D., Geissler, P.E., 1996. The formation of asteroidal satellites in large cratering collisions. *Bull. Am. Astron. Soc.* 28, 1101.
- Durda, D.D., Greenberg, R., Jedicke, R., 1998. Collisional models and scaling laws: a new interpretation of the shape of the main-belt asteroid size distribution. *Icarus* 135, 431–440.
- Durda, D.D., Flynn, G.J., Hart, S.D., Asphaug, E., 2002. Impact disruption of three ordinary chondrite meteorites. In: *Proc. Lunar Planet. Sci. Conf.* 33rd. Abstract 1535.
- Durda, D.D., Bottke, W.F., Enke, B.L., Asphaug, E., Richardson, D.C., Leinhardt, Z.M., 2003. The formation of asteroid satellites in catastrophic impacts: results from numerical simulations. In: *Proc. Lunar Planet. Sci. Conf.* 34th. Abstract 1943.
- Farinella, P., Davis, D.R., 1992. Collision rates and impact velocities in the main asteroid belt. *Icarus* 97, 111–123.
- Flynn, G.J., Durda, D.D., 2002. Do  $\sim 10 \mu\text{m}$  IDPs sample the bulk composition of their parent bodies? *Meteorit. Planet. Sci.* 37, A47.
- Funato, Y., Makino, J., Hut, P., Kokubo, E., Kinoshita, D., 2003. Kuiper-belt formation through exchange reactions. *Nature*. In press.
- Goldreich, P., Lithwick, Y., Sari, R., 2002. Formation of Kuiper-belt binaries by dynamical friction and three-body encounters. *Nature* 420, 643–646.
- Hartmann, W.K., 1979. Diverse puzzling asteroids and a possible unified explanation. In: Gehrels, T. (Ed.), *Asteroids*. Univ. of Arizona Press, Tucson, pp. 466–479.
- Hamilton, D.P., Krivov, A.V., 1997. Dynamics of distant moons of asteroids. *Icarus* 128, 241–249.
- Jedicke, R., Metcalfe, T.S., 1998. The orbital and absolute magnitude distributions of main belt asteroids. *Icarus* 124, 141–155.
- Jedicke, R., Larsen, J., Spahr, T., 2002. Observational selection effects in asteroid surveys and estimates of asteroid population sizes. In: Bottke, W.F., Cellino, A., Paolicchi, P., Binzel, R.P. (Eds.), *Asteroids III*. Univ. of Arizona Press, Tucson, pp. 71–87.
- Knežević, Z., Lemaître, A., Milani, A., 2002. The determination of asteroid proper elements. In: Bottke, W.F., Cellino, A., Paolicchi, P., Binzel, R.P. (Eds.), *Asteroids III*. Univ. of Arizona Press, Tucson, pp. 603–612.
- Leinhardt, Z.M., Richardson, D.C., 2002. *N*-body simulations of planetesimal evolution: effect of varying impactor mass ratio. *Icarus* 159, 306–313.
- Leinhardt, Z.M., Richardson, D.C., Quinn, T., 2000. Direct *N*-body simulations of rubble pile collisions. *Icarus* 146, 133–151.
- Melosh, H.J., 1989. *Impact Cratering: A Geologic Process*. Oxford Univ. Press, New York.
- Merline, W.J., Close, L.M., Dumas, C., Shelton, J.C., Ménard, F., Chapman, R.C., Slater, D.C., 2000. Discovery of companions to Asteroids 762 Pulcova and 90 Antiope by direct imaging. *Bull. Am. Astron. Soc.* 32, 1309.
- Merline, W.J., Close, L.M., Ménard, F., Dumas, C., Chapman, C.R., Slater, D.C., 2001. Search for asteroid satellites. *Bull. Am. Astron. Soc.* 33, 1133.
- Merline, W.J., Weidenschilling, S.J., Durda, D.D., Margot, J.L., Pravec, P., Storrs, A.D., 2002a. Asteroids do have satellites. In: Bottke, W.F., Cellino, A., Paolicchi, P., Binzel, R.P. (Eds.), *Asteroids III*. Univ. of Arizona Press, Tucson, pp. 289–312.
- Merline, W.J., Close, L.M., Siegler, N., Dumas, C., Chapman, C.R., Rigaut, F., Owen, W.M., Slater, D.C., Durda, D.D., 2002b. Discovery of a loosely-bound companion to main-belt Asteroid (3749) Balam. *Bull. Am. Astron. Soc.* 34, 201.
- Merline, W.J., Close, L.M., Tamblyn, P.M., Ménard, F., Chapman, C.R., Dumas, C., Duvert, G., Owen, W.M., Slater, D.C., Sterzik, M.F., 2003a. S/2003 (1509) 1. *IAU Circ.* 8075, 2.
- Merline, W.J., Tamblyn, P.M., Dumas, C., Close, L.M., Chapman, C.R., Ménard, F., 2003b. S/2003 (130) 1. *IAU Circ.* 8183, 1.
- Michel, P., Benz, W., Tanga, P., Richardson, D.C., 2001. Collisions and gravitational reaccumulation: forming asteroid families and satellites. *Science* 294, 1696–1700.
- Michel, P., Benz, W., Tanga, P., Richardson, D.C., 2002. Formation of asteroid families by catastrophic disruption: simulations with fragmentation and gravitational reaccumulation. *Icarus* 160, 10–23.
- Milani, A., Knežević, Z., 1994. Asteroid proper elements and the dynamical structure of the asteroid main belt. *Icarus* 107, 219–254.
- Nesvorný, D., Bottke, W.F., Dones, L., Levison, H.F., 2002. The recent breakup of an asteroid in the main-belt region. *Nature* 417, 720–722.
- Nesvorný, D., Bottke, W.F., Levison, H.F., Dones, L., 2003. Recent origin of the zodiacal dust bands. *Astrophys. J.* 591, 486–497.
- Petit, J.-M., Chambers, J.E., Franklin, F., Nagasawa, M., 2002. Primordial excitation and depletion of the main belt. In: Bottke, W.F., Cellino, A., Paolicchi, P., Binzel, R.P. (Eds.), *Asteroids III*. Univ. of Arizona Press, Tucson, pp. 711–723.
- Petit, J.-M., Morbidelli, A., Chambers, J.E., 2001. The primordial excitation and clearing of the asteroid belt. *Icarus* 153, 338–347.
- Richardson, D.C., Bottke Jr., W.F., Love, S.G., 1998. Tidal distortion and disruption of Earth-crossing asteroids. *Icarus* 134, 47–76.
- Richardson, D.C., Quinn, T., Stadel, J., Lake, G., 2000. Direct large-scale *N*-body simulations of planetesimal dynamics. *Icarus* 143, 45–59.
- Richardson, D.C., Leinhardt, Z.M., Melosh, H.J., Bottke Jr., W.F., Asphaug, E., 2002. Gravitational aggregates: evidence and evolution. In: Bottke, W.F., Cellino, A., Paolicchi, P., Binzel, R.P. (Eds.), *Asteroids III*. Univ. of Arizona Press, Tucson, pp. 501–515.
- Scheeres, D.J., Durda, D.D., Geissler, P.E., 2002. The fate of asteroid ejecta. In: Bottke, W.F., Cellino, A., Paolicchi, P., Binzel, R.P. (Eds.), *Asteroids III*. Univ. of Arizona Press, Tucson, pp. 527–544.
- Shoemaker, E.M., 1962. Interpretation of lunar craters. In: Kopal, Z. (Ed.), *Physics and Astronomy of the Moon*. Academic Press, New York, pp. 283–359.
- Tillotson, J.H., 1962. Metallic equations of state for hypervelocity impact. General Atomic Report GA-3216.
- Weidenschilling, S.J., 2002. On the origin of binary transneptunian objects. *Icarus* 160, 212–215.
- Weidenschilling, S.J., Paolicchi, P., Zappalà, V., 1989. Do asteroids have satellites? In: Binzel, R.P., Gehrels, T., Matthews, M.S. (Eds.), *Asteroids II*. Univ. of Arizona Press, Tucson, pp. 643–658.
- Zappalà, V., Farinella, P., Knežević, Z., Paolicchi, P., 1984. Collisional origin of the asteroid families: mass and velocity distributions. *Icarus* 59, 261–285.